Geochemistry, Geophysics, Geosystems

RESEARCH ARTICLE
10.1029/2020GC009044

Nanoscale Imaging of High-Field Magnetic Hysteresis in Meteoritic Metal Using X-Ray Holography

R. Blukis[1], B. Pfau[2], C. M. Günther[3], P. Hessing[2], S. Eisebitt[2,4], J. Einsle[5], and R. J. Harrison[6]

[1]GFZ German Centre for Geosciences, Potsdam, Germany, [2]Max-Born-Institut, Berlin, Germany, [3]Center for Electron Microscopy (ZELMI), Technische Universität Berlin, Berlin, Germany, [4]Institut für Optik und Atomare Physik, Technische Universität Berlin, Berlin, Germany, [5]School of Geographical and Earth Sciences, University of Glasgow, Glasgow, UK, [6]Department of Earth Sciences, University of Cambridge, Cambridge, UK

Key Points:
- X-ray holography enables magnetization of natural samples to be imaged with ~40 nm resolution and in applied magnetic fields up to ±1.1 T
- Meteoritic cloudy zone consists of strongly interacting single-domain particles with single-particle coercivities up to 1 T
- Average interaction fields between particles in the cloudy zone are of the order 100–200 mT

Supporting Information:
- Supporting Information S1
- Movie S1
- Movie S2

Correspondence to:
R. Blukis,
roberts.blukis@gfz-potsdam.de

Citation:
Blukis, R., Pfau, B., Günther, C. M., Hessing, P., Eisebitt, S., & Einsle, J., et al. (2020). Nanoscale imaging of high-field magnetic hysteresis in meteoritic metal using X-ray holography. *Geochemistry, Geophysics, Geosystems*, *21*, e2020GC009044. https://doi.org/10.1029/2020GC009044

Received 17 MAR 2020
Accepted 23 JUN 2020
Accepted article online 29 JUN 2020

Abstract Stable paleomagnetic information in meteoritic metal is carried by the "cloudy zone": ~1–10 μm-wide regions containing islands of ferromagnetic tetrataenite embedded in a paramagnetic antitaenite matrix. Due to their small size and high coercivity (theoretically up to ~2.2 T), the tetrataenite islands carry very stable magnetic remanence. However, these characteristics also make it difficult to image their magnetic state with the necessary spatial resolution and applied magnetic field. Here, we describe the first application of X-ray holography to image the magnetic structure of the cloudy zone of the Tazewell IIICD meteorite with spatial resolution down to ~40 nm and in applied magnetic fields up to ±1.1 T, sufficient to extract high-field hysteresis data from individual islands. Images were acquired as a function of magnetic field applied both parallel and perpendicular to the surface of a ~100 nm-thick slice of the cloudy zone. Broad distributions of coercivity are observed, including values that likely exceed the maximum applied field. Horizontal offsets in the hysteresis loops indicate an interaction field distribution with half width of ~100 mT between the islands in their room temperature single-domain state, providing a good match to first-order reversal curve diagrams. The results suggest that future models of remanence acquisition in the cloudy zone should take account of strong interactions in order to extract quantitative estimates of the paleofield.

Plain Language Summary Magnetic fields played a significant role in the formation of the solar system and the evolution of the early planetary bodies in the first few million years after solar system formation. Knowledge about magnetic fields in the early solar system can be obtained from meteorites. Some meteorite types contain abundant iron-nickel alloy that contains nanoscale "cloudy zone" regions (named after their appearance in an optical microscope) that can preserve magnetic information over 4.5 billion years. The cloudy zone is a complex material consisting of magnetically stable nanoscale particles embedded in a nonmagnetic matrix in very close proximity to one another. The fine scale and extreme magnetic stability of the cloudy zone make it challenging to study using conventional magnetic microscopy techniques. Here, we apply X-ray holography for the first time to image the magnetization of individual magnetic particles and how they respond to magnetic fields. This new approach enables us to measure the magnetic properties of individual nanoscale particles, providing the first direct measurement of their magnetic stability and the strength of particle interactions. These measurements will improve our understanding of the magnetic information carried by the cloudy zone, and of how to extract information about solar system magnetic fields.

1. Introduction

1.1. Magnetic Fields in the Early Solar System

Magnetic fields are thought to have played an important role in driving the inward transport of mass and outward transport of angular momentum during the evolution of the early solar system and are necessary to account for the high accretion rates of protoplanetary disks observed astronomically (Bai & Stone, 2013; Santos et al., 2018; Simon et al., 2013; Wardle, 2007). Nebula magnetic fields in our solar system were relatively short-lived, shutting down as the nebula gas dissipated ~4 million years (Myr) after the formation of calcium aluminum inclusions (CAIs) (Wang et al., 2017). A longer-lived source of magnetic fields in the early solar system comes from differentiated planetesimals, which are thought to have generated

magnetic fields driven by thermal and/or chemical convection within their liquid iron cores for tens or even hundreds of Myr after CAI formation. Evidence of both nebular and planetesimal fields is obtained from the meteorite record (Bryson et al., 2015; Fu et al., 2012, 2014). The ability to make quantitative paleomagnetic measurements of past magnetic fields from meteorites is an important tool for constraining astrophysical models of star system formation and the thermal, chemical, and physical properties of planetesimals.

Obtaining reliable paleomagnetic data from meteorites is made more difficult by the nature of their magnetic remanence carriers. Many planetesimals formed under highly reducing conditions, meaning that their magnetic mineralogy is dominated by iron-nickel metal (e.g., kamacite and taenite) with very different magnetic properties to the iron oxides (e.g., magnetite and hematite) that are the mainstay of terrestrial paleomagnetic studies. Magnetically soft kamacite (a ferromagnetic iron-nickel alloy with body-centered cubic structure) is common in many meteorites. The poor paleomagnetic recording properties of multidomain (MD) kamacite led many researchers to conclude that paleomagnetic measurements of metal-rich meteorites were not possible (Brecher & Albright, 1977; Guskova, 1965). New high-spatial-resolution "nanopaleomagnetic" methods, however, have enabled paleomagnetic information to be extracted from meteoritic metal. This approach uses X-ray photoemission electron microscopy (XPEEM) to target magnetic measurements at the "cloudy zone": ~1–10 μm-sized subregions of the metal that contain abundant single-domain (SD) particles (islands) of tetrataenite, a tetragonal form of ordered FeNi with exceptional magnetic stability. This method has been applied successfully to study meteoritic metal in iron and stony-iron meteorites, yielding paleomagnetic information that is not accessible by other techniques (Bryson et al., 2015, 2017, 2019; Nichols et al., 2016).

The three-dimensional chemical, crystallographic, and magnetic architecture of the cloudy zone has recently been studied using a combination of synchrotron Mössbauer spectroscopy (SMS), scanning transmission electron microscope (STEM) tomography, atom probe tomography (APT), scanning precession electron diffraction (SPED), and micromagnetic simulations (Blukis et al., 2017; Einsle et al., 2018). The cloudy zone consists of ~10–150 nm diameter islands of ferromagnetic tetrataenite embedded in a paramagnetic matrix of antitaenite, a metastable face-centered cubic (fcc) iron-nickel alloy containing ~15–25% Ni. Above 320°C, the FeNi islands adopt a disordered fcc structure (taenite). Taenite is a soft ferromagnet with low magnetocrystalline anisotropy, so that above 320°C the islands are predicted to adopt single-vortex (SV) states. Below 320°C, Fe and Ni atoms order onto alternating (002) layers of the parent fcc structure, yielding the tetragonal tetrataenite structure (space group P4/mmm). The transition to tetrataenite causes the SV state to transform to an SD state on account of its high uniaxial magnetocrystalline anisotropy (1.37×10^7 erg/cm^3; Néel et al., 1964). The transition from SV to SD occurs via a transient two-domain (2-D) state (Einsle et al., 2018). The uniaxial easy axis of tetrataenite corresponds to the tetragonal *c* axis, normal to the Fe-Ni layering, which in turn corresponds to one of the three <100> cubic directions of the parent taenite. The magnetic switching field of tetrataenite is predicted to be very high and has been estimated to be close to 2 T (Néel et al., 1964). Magnetic properties of tetrataenite, as measured experimentally in meteorite and artificial samples (Bryson, Church, et al., 2014; Gattacceca et al., 2014; Néel et al., 1964), indicate the magnetic structure in the cloudy zone is highly stable with respect to remagnetization and therefore a very useful material for paleomagnetic studies.

Although the magnetic structure of the cloudy zone is very stable, it is not easy to interpret. In their SV state above 320°C, taenite islands are weakly to moderately interacting (Einsle et al., 2018). It has been postulated that these interactions play a fundamental role in the process of acquiring remanence (Yeem & Harrison, 2019). After the transition from taenite to tetrataenite below 320°C, SV islands are initially converted to a 2-D state with a small net moment (Einsle et al., 2018). Weak interactions between neighboring 2-D islands, combined with the external applied field, cause domain walls to shift, thereby increasing the net moment of each island. This increased moment enhances the interaction fields, resulting in even greater domain wall displacement. A positive feedback effect causes the majority of domain walls to be driven out of the islands, creating a magnetically biased population of strongly interacting SD states. According to this hypothesis, quantifying and modeling interactions will be necessary to reconstruct accurate and reliable absolute paleointensity data. Current methods used to estimate paleointensity from measurements of cloudy zone magnetization (Maurel et al., 2019) do not account for interactions. Although such methods are sufficient to determine the presence or absence of a magnetizing field, and to provide a relative comparison of

paleointensities between samples with different cooling rates, absolute paleointensities will possibly be inaccurate. Methods to simulate the remanence acquired by interacting SD particles have been developed and successfully applied to meteorites (Muxworthy, 2013; Muxworthy et al., 2011; Shah et al., 2017). These methods use first-order reversal curve (FORC) diagrams to characterize the interactions between particles. However, since the cloudy zone forms a volumetrically very small part of the metal in meteorites, using FORCs to characterize the intracloudy zone interactions is not straightforward. The magnetic signal from the cloudy zone is very hard to separate from much stronger signals of kamacite and plessite. FORC diagrams of tetrataenite-bearing meteoritic metal show complex patterns that are poorly understood and strongly affected by interactions between the kamacite, plessite, and cloudy zone components of the metal. For these reasons, a spatially resolved, high-field magnetic imaging method is desirable, as it enables the magnetic interactions between particles in the cloudy zone to be determined directly via the horizontal shift of the hysteresis loops.

1.2. X-Ray Holography

X-ray holography is well suited for examination of the cloudy zone, as it can image sample magnetization with a spatial resolution of ~20–40 nm, sufficiently high to resolve individual tetrataenite islands (Eisebitt et al., 2004). Methods previously used to examine magnetic particles in geological samples, such as electron holography, magneto-optical Kerr microscopy, and magnetic force microscopy, image magnetic induction or stray fields (Faigel & Tegze, 1999; Qiu & Bader, 2000; Sarid, 1994; Shah et al., 2018). Inverting magnetic induction or stray fields to yield the underlying magnetization is difficult and often nonunique. Images also cannot be obtained during application of magnetic fields stronger then few tens of mT, which means only remanence states can be imaged. X-rays image magnetization directly by exploiting the X-ray magnetic circular dichroism (XMCD) effect and are not affected by stray fields. There are other methods, such as XPEEM, that can achieve similar spatial resolution. However, as this method is based on imaging electrons emitted from the sample surface, imaging cannot be performed under application of strong magnetic fields. While other X-ray microscopy methods such as X-ray transmission microscopy (TXM) and scanning transmission X-ray microscopy (STXM) achieve a similar resolution to X-ray holography and have also been used to study magnetic properties of meteoritic samples (Nichols et al., 2019), holography is inherently unaffected by mechanical drifts, as the X-ray optics and the sample are monolithically interfaced to each other. The lack of image drift allows precise tracking of the magnetization of nanometer-scale particles during high-field hysteresis cycling. In addition, the tight space constraints in STXM and TXM instruments, given by the positioning of sample and X-ray optics, impede the assembly of (electro)magnets and again limit the maximum available magnetic field to typically 200–500 mT (Kim et al., 2006; Nolle et al., 2012). Overall, this makes X-ray holography very applicable in practice for sample examination under strong magnetic fields. X-ray holography has not been previously applied to study magnetic properties of any geological sample. However, its capabilities have been successfully demonstrated on various artificial materials such as patterned and continuous magnetic thin films as well as magnetically capped nanospheres (Büttner et al., 2017; Eisebitt et al., 2004; Günther et al., 2010; Hellwig et al., 2006; Pfau et al., 2014). In particular, X-ray holography was used to reveal the stray-field interaction in ordered arrays of nanometer-sized magnetic islands (Pfau et al., 2014). The flexibility and robustness of the holography setup even allows in-field imaging with variable temperature (Hauet et al., 2008)—an environmental combination that is challenging for other imaging methods. However, the inherently drift-free apparatus comes at the price of a fixed field of view (FOV) during the experiment and elaborate sample fabrication, typically, using focused-ion beam (FIB) preparation techniques.

X-ray holography is a full-field, lensless imaging technique. The coherent far-field diffraction from the sample is directly recorded by a 2-D detector without any focusing (i.e., imaging) optics in between. As the detector only detects the intensity information of the diffracted radiation and the phase information is lost, the coherent diffraction pattern cannot be directly inverted to a real-space image of the sample. Holography solves this so-called phase problem by interfering the diffracted radiation from the sample with a known reference wave. In the interference pattern (the hologram) between both waves, the relative phase differences are translated to detectable intensity variations. Typically, the reconstruction of the real-space image from the hologram is carried out digitally. In the case of Fourier-transform holography, which is applied

here and which employs a spherical reference wave, the reconstruction is performed by a simple Fourier transformation of the hologram.

The principle of mask-based X-ray holography is to prepare the sample and the beam-splitting holography optics on the same X-ray transparent membrane substrate (Pfau & Eisebitt, 2015). The sample is mounted on the backside of the membrane and has to be thin enough to be investigated in transmission geometry (typically thinner than 100 nm). The membrane's frontside is coated with Au making it opaque to X-rays. The holography optics comprises of two apertures in the Au film. A micrometer-sized (1–5 μm in diameter), typically circular, aperture, which defines the sample FOV, is milled through the Au coating while leaving the sample intact. Adjacent to this, a small 30–50 nm aperture, the so-called reference hole (or holes), is milled through both the Au coating and the sample. This hole acts as the source for the reference wave needed for holography. The combined object, consisting of sample aperture and reference hole(s), is exposed to a coherent beam of X-rays. The distance between the sample aperture and the reference hole must not exceed the spatial coherence length of the X-rays but has to be large enough (at least larger than the 1.5 fold FOV diameter) to ensure a clear separation of the images in the numerical reconstruction. The waves transmitted through the apertures interfere to produce a far-field diffraction pattern (X-ray hologram) that is recorded on a 2-D detector placed downstream of the sample. The detector size and its distance from the sample define the maximum detection angle, that is, the detector's numerical aperture (NA). The NA constitutes the first limit for the spatial resolution achievable. The digital inverse Fourier transformation (IFT) of the X-ray hologram yields the autocorrelation of the combined object, consisting of a central sample-sample autocorrelation and off-center images of sample-reference cross correlations. Therefore each sample-reference cross correlation contains an image of the sample that is blurred by the reference hole. The reference hole, thus, defines the second limiting factor for the spatial resolution of the image similar to its diameter. The final image of a sample is produced by cropping the sample-reference cross correlation from the IFT image and can be used for further analysis. As the sample aperture and reference hole are fixed relative to each other, the position of the reconstructed image is not affected by drift of the sample assembly, making the alignment of the resulting images very accurate (Büttner et al., 2015). To obtain magnetic contrast in the images, X-ray holograms are recorded using left- and right-circularly polarized X-rays at resonance with a suitable absorption resonance, and the difference is used to calculate the XMCD signal. Imaging with XMCD-based contrast is only sensitive to the magnetization component parallel to the X-ray propagation direction. In case of X-ray holography in the standard transmission geometry, this is the out-of-plane (m_z) component. The theory of the holography method in detail has been described elsewhere (Eisebitt et al., 2004; Pfau & Eisebitt, 2015; Stroke, 1965; Winthorp & Worthing, 1965).

2. Materials and Methods

2.1. Sample Description and Preparation for X-Ray Holography

A small sample of Tazewell IIICD iron meteorite (Sample 16269) was provided by the Sedgwick museum of Earth Sciences, University of Cambridge, UK. This sample was selected, as it shows a typical cloudy zone with medium to large maximum average island size of 92 nm (Yang et al., 1997). The meteorite and the sample were also considered to be well understood due to multiple previous studies (Blukis et al., 2017; Bryson et al., 2017; Bryson, Church, et al., 2014; Einsle et al., 2018; Scott, 1973; Yang et al., 1997). X-ray holography sample preparation requires placing a soft X-ray transparent lamella of the meteorite onto an X-ray holography sample holder. The sample holder consisted of a silicon chip with 200 nm thick silicon nitride (Si_3N_4) membrane windows used as substrate for X-ray imaging. The entire sample holder was coated with a multilayer consisting of 20 repeats of Cr (5 nm)/Au (55 nm) fabricated by thermal evaporation. At this thickness, the multilayer is opaque to soft X-rays at the iron L_3-absorption edge. A multilayer coating was chosen, as it ensures better sputtering homogeneity during FIB milling of the aperture. A circular aperture with diameter of 5.3 μm was milled in the gold layer on top of the membrane window. Reference holes with a diameter of 40–80 nm were milled next to the aperture through the gold and Si_3N_4 membrane. For aperture milling, a FEI HELIOS 600 Nanolab (ZELMI, TU Berlin) was used.

To prepare the lamella, the meteorite sample surface was mechanically polished using diamond suspensions with the final diamond particle size of 0.25 μm. A lamella of the cloudy zone was prepared using FEI Helios Nanolab Dual Beam FIB and scanning electron microscope (SEM) of the Department of Material Science

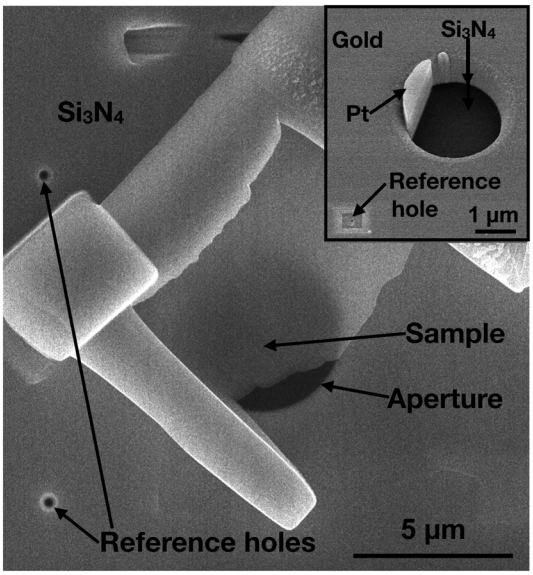

Figure 1. An ~60–100 nm thick lamella of the Tazewell meteorite on a silicon nitride membrane prepared for an X-ray holography experiment. The inset shows the reverse side (gold side) of the sample holder chip. The sample did not cover the entire aperture, and the excess X-rays allowed through the aperture were stopped by platinum deposited on the reverse side of the sample. Only a single reference hole was used. Other holes in the gold coating were covered with platinum on the reverse side.

and Metallurgy, University of Cambridge, UK, using standard techniques (Schaffer et al., 2012). The lamella was polished using the ion beam to a thickness of 50–100 nm using a procedure by Schaffer et al. (2012). The lamella was then welded using ion-beam platinum deposition to the Si_3N_4 membrane on top of an aperture on the other side (inset Figure 1).

2.2. X-Ray Holography Experiment

X-ray holography was performed at the UE52-SGM undulator beamline of the BESSY II synchrotron-radiation facility in Berlin, Germany. The sample was illuminated with circularly polarized soft X-rays tuned to the Fe L_3 absorption edge at 707 eV (1.75 nm wavelength). The silicon nitride sample holder was mounted on a larger Al holder and lowered into a high-vacuum chamber. The far-field diffraction pattern was recorded by a CCD detector (Greateyes, 2,048 × 2,048 pixels, 13.5 μm pixel size) situated 31.5 cm behind the sample. A beamstop was used to protect the detector from the intense central peak of transmitted and forward-scattered X-rays. The external magnetic field was applied using an electromagnet with four poles arranged in four quadrants around the sample. By changing magnetization at each pole, the magnetic field could be applied in-plane or out-of-plane relative to the sample surface. The maximum field strength achievable with the electromagnets used was ~1.05 T. A schematic drawing of the setup is presented in the supporting information (Figure S2).

Two hysteresis measurements were made, with the magnetic field applied out-of-plane and in-plane relative to the sample surface. Note that also, for the in-plane magnetic field orientation, only the out-of-plane magnetization component is imaged. In each hysteresis loop 32 images of magnetization were taken with an average spacing between the applied field steps of ~0.1 T. Acquisition of each image required two holograms recorded at opposite beam helicities (an example hologram can be found in the supporting information). The raw images were processed to obtain the final images of magnetization at each field step. The processing involved first removing artifacts caused by cosmic rays and background radiation that appear as very high intensity signals on individual pixels scattered randomly through the detector. After that, saturated areas, edges of the beamstop, and supporting wires were smoothly masked. A high-pass filter was then applied to remove noise, and the raw hologram was then centered. The difference between the holograms for left- and right-polarized light was then calculated to extract XMCD information. A real-space image is then obtained via a 2-D IFT. Propagation of the reconstructed complex image (reflecting both amplitude and phase information) to the plane where the reference beam has the smallest waist was performed in order to enhance the spatial resolution of the reconstructed image (Geilhufe et al., 2020). This was followed by phase-ramp compensation to suppress artifacts due to sample thickness variations over the FOV. A cross correlation containing the magnetic image of the sample was then cropped out and used for analysis. The phase was then rotated to obtain maximum magnetic contrast in the real part of the waist reconstruction. For visualization only, the image was linearly interpolated to be four times larger in size. Note that the in-plane hysteresis loop shows significantly more image noise at the end of the loop when returning to negative applied field. This noise is caused by a reduced overall signal due to drift of the whole setup away from the incoming beam's intensity maximum and due to carbon contamination of the sample after

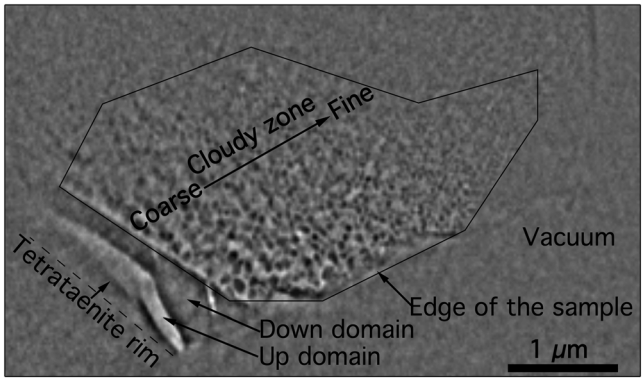

Figure 2. A representative image of the magnetization (out-of-plane component) of the cloudy zone. White pixels indicate magnetization out of the plane of the diagram; black pixels indicate magnetization into the plane of the diagram. This image has been obtained at −0.6 T applied magnetic field in out-of-plane geometry.

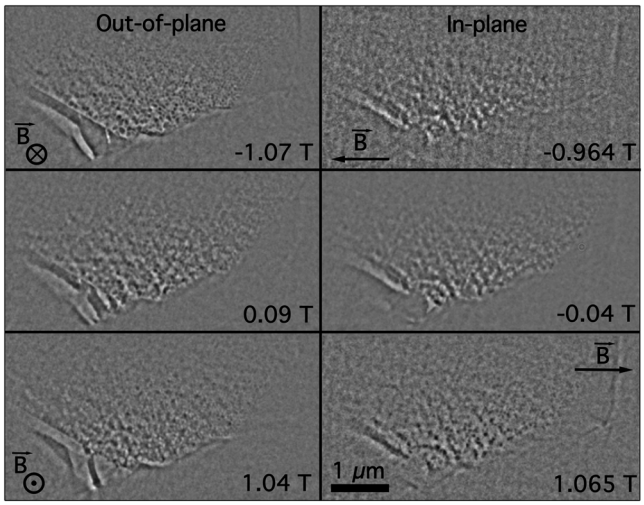

Figure 3. A sequence of images from the hysteresis loops with the magnetic field applied out-of-plane (left) relative and in-plane (right) to the sample surface. White pixels indicate magnetization out of the plane of the diagram (positive direction); black pixels indicate magnetization into the plane of the diagram (negative direction). During hysteresis loop acquisition, the applied field was changed from negative to positive and back to negative saturation. The images at 0.09 and −0.04 T represent the approximate remanence states after negative saturation. B indicates the applied field direction. For a full sequence of all magnetic images obtained in both hysteresis loops, see the supporting information.

long automatic hysteresis scans. In the holographic geometry, this drift *does not* translate to a position drift of the reconstructed image.

2.3. Simulations Using FORCulator

FORC diagrams of an interacting ensemble of SD tetrataenite islands were simulated using the FORCulator code (Harrison & Lascu, 2014). The cloudy zone was modeled as an assemblage of 100 spherical particles, each 70 nm in diameter, randomly dispersed in a cubic box with packing fraction 50%. This corresponds approximately to the center of the experimentally measured region. Each particle was given a random coercivity picked from the distribution of coercivities observed experimentally in the X-ray holography out-of-plane data set. Easy axes were assigned randomly to the three possible <100> directions. Each simulation contained 100 individual FORCs with a field step size of 0.0025 mT. The conversion from individual FORCs to the final FORC diagram was performed according to the methodology described in Harrison and Lascu (2014). The results presented represent the average of 100 separate simulations, each generated with a random placement of particles and easy axes, and a new random assignment of coercivities from the distribution observed in X-ray holography.

3. Results

3.1. X-Ray Holography

In total, 32 magnetization images were obtained in both in-plane and out-of-plane hysteresis loops (see Figure 2 for a representative example of a single image and Figure 3, for a selected image sequence). The magnetic field was changed from approximately −1 to ~1 T back to approximately −1 T. The images within hysteresis series are inherently

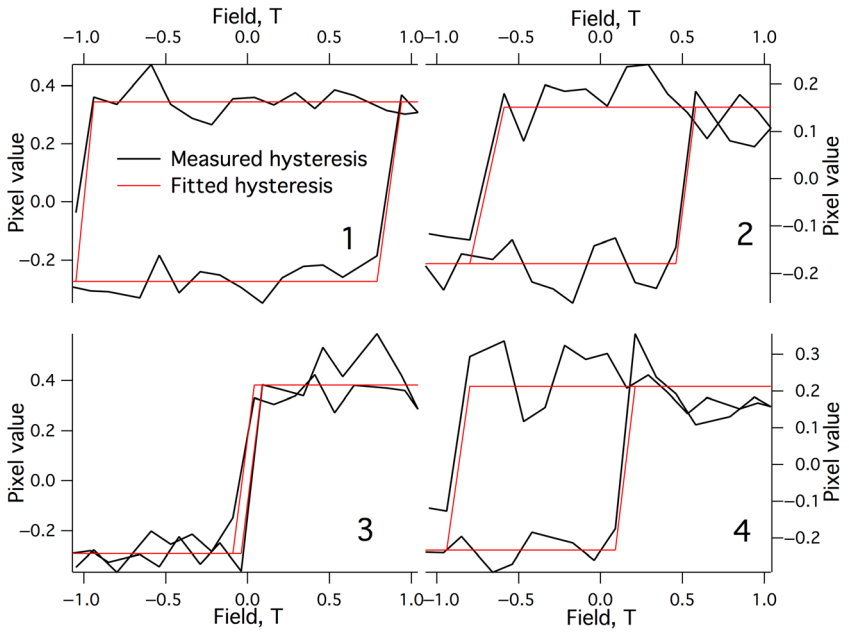

Figure 4. Four representative single-pixel hysteresis loops of the out-of-plane data set. Significant variability in coercivities and offset values was observed. The loops were fitted, assuming that each island is a single-domain with only two allowed magnetization directions. The positions of the islands corresponding to these hysteresis loops are shown in Figures 6a and 6c.

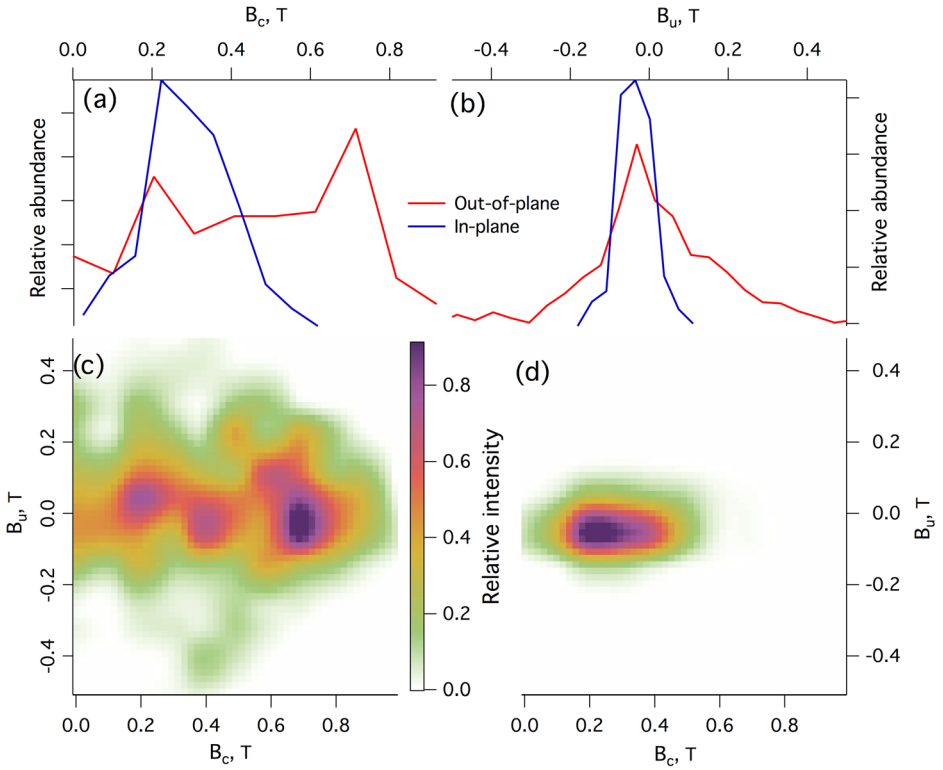

Figure 5. (a) Histograms of coercivity (B_c) and (b) horizontal offset (B_u) for the out-of-plane and in-plane data sets. (c and d) Measured Preisach (FORC-like) distributions of the sample with the magnetic field being applied out-of-plane (c) and in-plane (d). Preisach diagram images have been bilinearly interpolated to five times larger size and smoothed.

aligned to each other in terms of translational image drift. Only sample rotation had to be corrected; however, this was negligible in almost all images. Full sequence of magnetic images from both hysteresis loops is attached to the supporting information as mp4 files. Each pixel represents sample magnetization at that specific location throughout the magnetic field images. Hence, a hysteresis loop of each pixel can be extracted. The pixel size in the magnetization images was 20 nm × 20 nm. Hysteresis loops were observed to often change very rapidly in appearance from one pixel to the next; therefore, the spatial resolution was inferred to be diffraction limited to 40 nm. The hysteresis loops of the tetrataenite islands are expected to show square hysteresis behavior, with islands switching between two magnetization states (Figure 4). Although many pixels did show this behavior, a significant number of pixels showed complex or distorted hysteresis loops. Simulated images of hypothetical cloudy zone structures demonstrated that this effect was primarily caused by overlapping islands and a large matrix contribution to the signal, although the presence of some 2-D islands cannot be ruled out. Some anomalous "inverted" hysteresis loops were also observed and were excluded from analysis as they arise under certain conditions as a consequence of using a beamstop in the experiment. The beamstop blocks the central peak of the far-field diffraction pattern and effectively acts as a high-pass filter removing spatially slow variations in the magnetization. This means the island magnetization is measured relative to the immediate surroundings and can lead to apparently inverted hysteresis loops in the case of low-magnitude magnetization. This artifact has been simulated and demonstrated not to affect the results elsewhere (Blukis, 2018). Each pixel was examined manually, and only pixels that showed clear two-state hysteresis behavior with noise level such that up and down domain magnetization values did not overlap were selected for analysis. Pixels with very noisy, unusual, complex, or inverted hysteresis loops were not analyzed further.

To analyze the individual hysteresis loops, a folded square wave was fitted to the measured loop using least squares fitting (Figure 4). The square wave is defined by two critical switching fields, B_a and B_b, which correspond to the fields needed to switch from the upper to the lower branch and from the lower to the upper branch of the hysteresis loop, respectively.

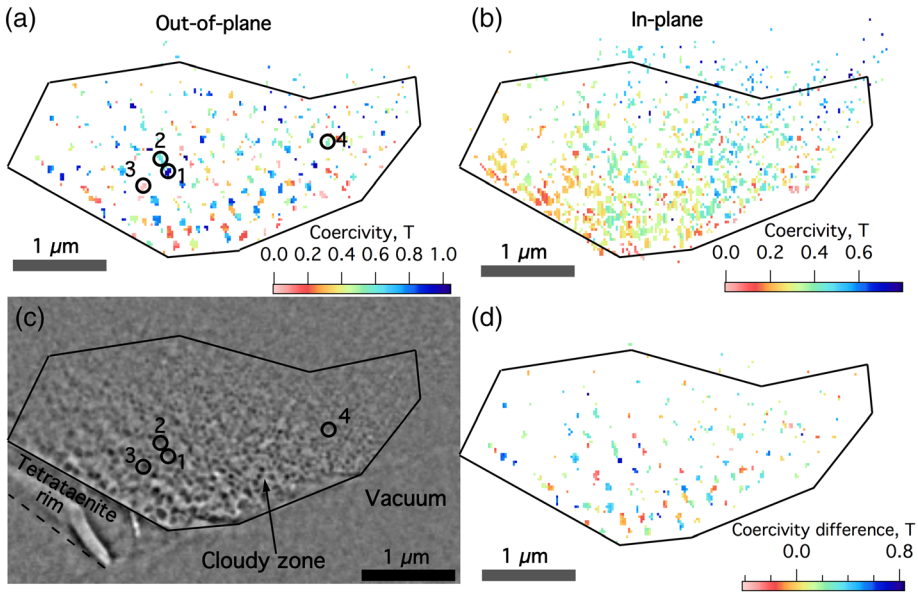

Figure 6. (a) Map of coercivities in the out-of-plane data set. (b) Map of coercivities in the in-plane data set. This data set shows systematic increase in coercivity with decreasing particle size. (c) Magnetic image of the sample, numbered circles indicate positions of the hysteresis loops shown in Figure 4. (d) Map of coercivity differences between the out-of-plane and in-plane data sets where good hysteresis loops could be obtained in both datasets.

The coercivity $B_c = (B_b - B_a)/2$ and horizontal offset $B_u = (B_b + B_a)/2$ values were then calculated from these fitted loops. According to conventional Preisach interpretation, the horizontal offset is equated with the interaction field acting on the island. Average B_c and B_u values, as well as distributions (Figures 5a and 5b), were calculated from the individual pixel data. The coercivity and offset data allow Preisach diagrams to be generated (see Figures 5c and 5d). These diagrams contain similar information to a FORC diagram, especially in a system consisting of SD particles with square hysteresis loops. In total 885 pixels were analyzed in the out-of-plane and 2,108 pixels in the in-plane hysteresis data sets. The average coercivity of the tetrataenite islands was calculated to be 0.5 T in the out-of-plane data set and 0.4 T in the in-plane data set. The distribution of coercivities in the out-of-plane data set is very broad (Figure 5a), with some islands having values in excess of 0.8 T. The offset distribution peaks near zero field in both data sets, and although the in-plane data set shows an average value toward slightly negative values, this is within error of zero. The errors in coercivity and offset are estimated to be 0.05 T and were estimated from the average field step of 0.1 T. Offset distributions in both experiments are not consistent with simple Gaussian or Lorentzian distributions (Figure 5b).

The spatial distribution of analyzed pixels was random throughout the cloudy zone in the out-of-plane data set (Figure 6a). The in-plane data set, on the other hand, has a higher density of analyzed pixels in the coarse cloudy zone (Figure 6b). There is a systematic decrease in coercivity (Figure 6b) with increasing island size (Figure 6c) in the in-plane data set, so the resulting coercivity distribution (Figure 5b) may be slightly biased toward lower values. The offset distributions are unaffected by this effect, as offset values show no correlation with position or island size in either data set. Islands were observed to have significantly different coercivities depending on the measurement geometry (see Figure 6d).

3.2. FORCulator Results and Comparison With the Experiment

FORCulator simulations using the experimentally measured coercivity distribution from the out-of-plane data set produced similar offset distributions to those observed using X-ray holography, although the distribution was narrower and more similar to that observed in the in-plane data set. The simulations also showed a diffuse cloud of signal in the coercivity range of 0.2–0.6 T (Figure 7a) similar to features the experimentally measured Preisach diagram in the slightly larger coercivity range 0.1–0.8 T (Figure 7b).

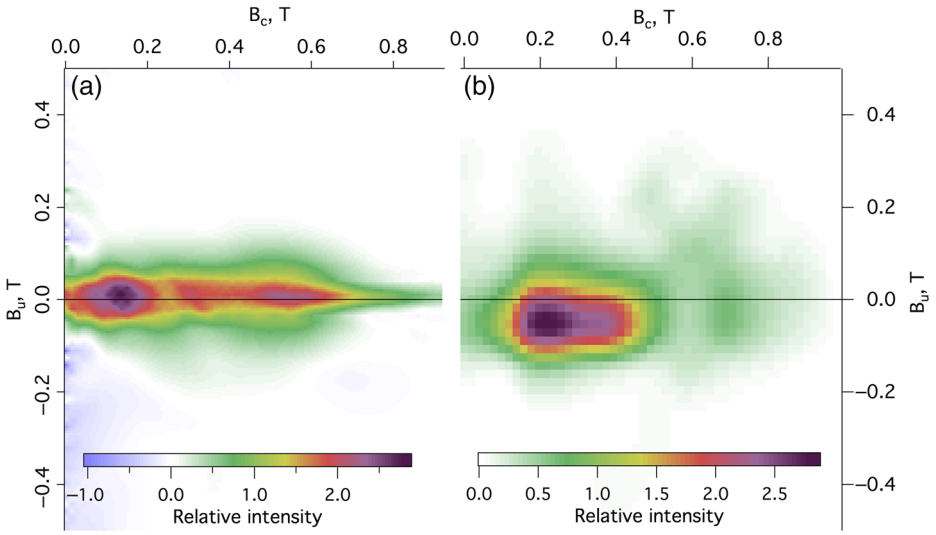

Figure 7. (a) A simulated FORC diagram using FORCulator code. (b) A combined Preisach distribution of both in-plane and out-of-plane data sets. Preisach distributions of both data sets were assigned an equal total weighting and rescaled to a comparable intensity to the FORC diagram obtained using FORCulator for comparison. The Preisach distribution (b) has been interpolated to five times larger size and smoothed, processing of the FORC diagram shown in (a) is described in methods.

Figure 8 shows four different offset distributions, three experimental and one simulated using FORCulator (Harrison & Lascu, 2014). The offset distributions of FORC diagrams were obtained by projecting the FORC diagrams onto the B_u axis. However, as FORC distributions and Preisach distributions are in general not equivalent; there are features in the experimental FORC distribution that need to be understood before this projection can be interpreted as an offset distribution. The sample of Marjalahti pallasite contains not only the cloudy zone but also kamacite and plessite. Due to experimental constraints, the FORC diagram does not extend further than 0.18 T on the B_u axis. The central feature in the FORC diagram did, within experimental

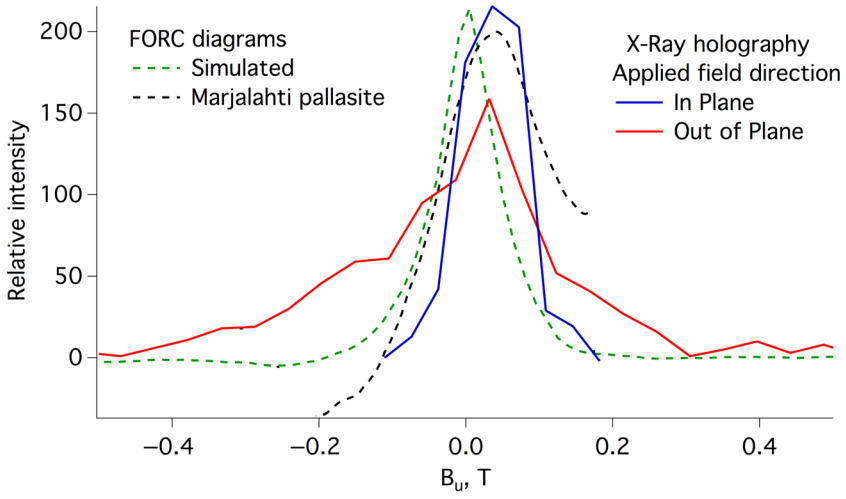

Figure 8. Offset distributions measured in the X-ray holography experiment (red and blue lines). Green dashed line represents the simulated offset distribution using FORCulator (extracted from FORC diagram showed in Figure 7a). Offset distribution is also shown for an experimentally measured FORC diagram of the Marjalahti pallasite (Nichols et al., 2016). The intensities of both FORC distributions were adjusted to be comparable to the histograms extracted from X-ray holography data sets. To make comparison between offset distributions easier, the two offset distributions extracted from X-ray holography are reversed. This was considered appropriate since they are extracted from Preisach and not FORC distributions.

error, match the broadness of the offset distribution observed in the X-ray holography experiment. The peak in the offset distribution is located a similar distance away from zero as the offset distributions measured in X-ray holography. The in-plane and out-of-plane data sets demonstrate different offset peak broadness and shape. The experimental FORC is approximately in-between the two in terms of its offset distribution and probably represents the effect of orientation averaging in the experimental FORC measurement. The major difference between in-plane and out-of-plane data sets is the much narrower offset distribution in the in-plane data set. If the ~0.05 T offset from zero in the X-ray holography data is ignored, the simulated offset distribution using FORCulator is also a close match to the measured offset distribution in the in-plane data set most likely due to lower contribution of demagnetizing field of a thin sample that is present in the out-of-plane data set. The offset from zero could be caused by a coarse field sampling step of ~0.1 T that was used in the X-ray holography experiment. Finer sampling would more accurately describe the hysteresis loops and therefore more accurate coercivity and offset values. This is more important for offsets, as the magnitudes of offset values are significantly smaller than the coercivity values and are therefore more susceptible to such errors.

4. Discussion

The coercivity distribution of the out-of-plane sample (Figure 5a) displays peaks in the histogram at 0.2 and 0.7 T. This is most likely due to the limited number of easy axis directions of tetrataenite in the cloudy zone. Tetrataenite islands adopt a tetragonal easy axis along one of the three <100> directions of the parent fcc structure. In our case, it was found by electron backscatter diffraction that the sample consists of a single fcc crystal and the <100> directions form angles of ~73°, 57°, and 37° to the applied field direction (normal to sample surface) (Figure S3). The significantly different angles between the easy axes of tetrataenite and the applied field are likely the cause of certain coercivity values being more prevalent than others. In the Preisach diagram (Figure 5c) three higher intensity regions can be seen that are possibly caused by the three different sets of easy axes. However, this is not the only factor affecting the observed coercivity, as all coercivity values between ~0 and ~1 T were observed. No such effects have been observed in the in-plane data set. The in-plane data set is heavily influenced by the presence of a ferromagnetic matrix that appears in thin lamellar samples due to a change in electronic ground state from low-moment ferrimagnetic to high-moment ferromagnetic state (Blukis et al., 2017) and therefore could be considered less representative of unaltered bulk cloudy zone that contains a paramagnetic matrix. The effect of a ferromagnetic matrix, as well as that of lamellar geometries, was explored by micromagnetic simulations and is reported in the supporting information. The key effect of the ferromagnetic matrix is to aid the formation of domain walls and reduce the barrier for them to penetrate the tetrataenite islands, thereby reducing the coercivity dramatically. This reduction in coercivity is more pronounced for in-plane fields than the out-of-plane fields when the truncated geometry of the islands is taken into account.

While it is theoretically possible that the coercivity difference between the two data sets (see Figures 5a and 6d) is caused by a majority of islands having an easy axis such that lower coercivities are observed in the in-plane data set, this is considered highly unlikely, as an area of cloudy zone as large as the one studied here is expected to have easy axes distributed nearly equally among the three possible choices as has been shown in previous studies (Bryson, Church, et al., 2014; Bryson, Herrero-Albillos, et al., 2014; Einsle et al., 2018). A highly biased easy-axis distribution would not explain why a systematic and island size-dependent variations in coercivity are observed only in the in-plane data set and not also in the out-of-plane data set.

As the simulations using FORCulator do not account for the impact of the ferromagnetic matrix, they are more representative of a bulk cloudy zone. FORC diagrams of meteoritic metal, such as the one previously published of the Marjalahti pallasite (Nichols et al., 2016), commonly show a weak, broad diffuse horizontal ridge. The ridge is similar to that normally associated with SD particles but is a lot broader. Based on the Preisach distributions obtained in this work, this diffuse ridge can be unambiguously attributed to the strongly interacting islands of tetrataenite in the cloudy zone. The offset values observed in the FORC diagram of the bulk meteorite (Marjalahti pallasite) sample (Figure 8) are slightly wider than those calculated using FORCulator and the in-plane data set, however, and are narrower than those observed in the out-of-plane data set. The two X-ray holography data sets show very different offset distributions and while, due to the effects of the ferromagnetic matrix, the in-plane data set could be disregarded as nonrepresentative, it is

also likely that the out-of-plane data set represents the opposite extreme. Despite this, the out-of-plane data set is considered to be more representative, as the influence of the artificially induced magnetization of the matrix is minimized. By using the coercivities observed in the out-of-plane data set, FORCulator predicts an offset distribution that is narrower than the one observed using X-ray holography. This indicates the interaction fields experienced by the islands in the actual cloudy zone are higher than those simulated. As the magnetic properties used to simulate particles in the cloudy zone have been experimentally observed in tetrataenite, the most likely source of discrepancy is the description of the cloudy zone as randomly positioned spherical particles with a packing fraction of 50%, which might not be entirely representative of the real cloudy zone. In the cloudy zone, both the packing fraction and the island shape will be different. This has been previously observed using electron tomography (Einsle et al., 2018) and shows the islands may have elongated, bent, and partially matching or interlocking shapes that would increase one islands exposure to the magnetic field produced by another. This would result in significantly higher interaction field. Nevertheless, simulations using FORCulator demonstrate that magnetostatic interactions are significant in systems like the cloudy zone and can be simulated to a relatively high accuracy. Provided appropriate particle geometries and packing fractions could be provided, for example, by performing a simulated spinodal decomposition, the FORC diagram calculated is very likely to be consistent with observations made using X-ray holography.

5. Conclusions

X-ray holography has been used to directly measure the in-field hysteresis behavior of nanoscale paleomagnetic remanence carriers in a meteoritic cloudy zone. The inherently drift-free holography setup allows the magnetization of single sub-100 nm particles to be observed through a full hysteresis cycle in different applied field directions and in fields of more than ± 1 T.

The cloudy zone contains numerous interacting SD particles at room temperature. This explains the diffuse high-coercivity signal seen in FORC diagrams of bulk samples. Most of the individual islands show high coercivities, implying high stability and confirming that a stable remanence can be carried by the cloudy zone. However, it was also shown by this experiment that interactions between particles are strong and should be considered explicitly in future models of remanence acquisition by the cloudy zone. Existing studies of remanence acquisition in the presence of interactions (Muxworthy et al., 2011; Shcherbakov et al., 1995; Shcherbakov & Sycheva, 1996) apply only to weakly interacting samples with magnetic particle packing fractions of a few percent. This is a significant difference from the cloudy zone, where the packing fraction of the magnetic tetrataenite islands is ~20–60% by volume (Einsle et al., 2018). On the basis of micromagnetic simulations, Einsle et al. (2018) argued that the cloudy zone acquires magnetization during the chemical ordering transition of taenite islands into tetrataenite, involving a domain-state transition from SV to 2-D to SD. In those simulations, the existence of strong interactions, biased by the presence of an applied magnetic field, played a key role in driving domain walls out of the tetrataenite islands, resulting in the 2-D to SD transition. Preliminary reports of models based on this hypothesis (Yeem & Harrison, 2019) demonstrate promising results, with a bias in the magnetic population of SD islands predicted that is similar to that observed experimentally and increasing linearly with applied field. However, more detailed work and modeling are required to fully understand the process and reconstruct quantitative paleointensity data. Although a complicated task, the ultimate reconstruction of quantitative paleointensity from the meteoritic cloudy zone would enable more accurate and complete insight into planetary body and system evolution processes.

This experiment demonstrates the feasibility of applying X-ray holography to directly image the magnetization of natural samples with a spatial resolution of 40 nm. Furthermore, such imaging can be performed under high external applied magnetic fields; therefore, in-field behavior of paleomagnetic remanence carriers can be directly studied. The method avoids the drawbacks of other nanoscale magnetic imaging methods such as electron holography or magnetic force microscopy by using an imaging probe that allows magnetization to be directly imaged. This is also an improvement over other X-ray methods such as XPEEM and transmission X-ray microscopy, as there is very little image drift as a function of applied field, making the extraction of high-resolution hysteresis loops on a pixel-by-pixel basis more reliable. X-ray holography could be used in the future to examine complex natural magnetic materials like magnetite-ulvöspinel

or titanomagnetite-titanohematite intergrowths, where it could enable imaging at higher applied fields and under varying applied field geometries, thereby providing complementary information to what is achievable with electron holography. Magnetic in-field behavior of other naturally occurring particles such as vortex state particles or particle chains could also be examined.

Conflict of Interests

The authors declare no conflict of interests.

Data Availability Statement

Data used in this study are available online (at zenodo.org/record/3709017).

Acknowledgments
This work was supported by the European Research Council under the European Union's Seventh Framework Programme (FP/2007-2013)/ERC Grant Agreement 320750 and 312284. We thank the Sedgwick Museum, University of Cambridge, for the sample of Tazewell meteorite.

References

Bai, X. N., & Stone, J. M. (2013). Local study of accretion disks with a strong vertical magnetic field: Magnetorotational instability and disk outflow. *Astrophysical Journal*, *767*, 1–18.

Blukis, R. (2018). *A combined experimental and computational study of nanopaleomagnetic recorders in meteoritic metal*. Cambridge, UK: University of Cambridge.

Blukis, R., Rüffer, R., Chumakov, A. I., & Harrison, R. J. (2017). A high spatial resolution synchrotron Mössbauer study of the Tazewell IIICD and Esquel pallasite meteorites. *Meteoritics & Planetary Science*, *52*(5), 925–936. https://doi.org/10.1111/maps.12841

Brecher, A., & Albright, L. (1977). The Thermoremanence hypothesis and the origin of magnetization in iron meteorites. *Journal of Geomagnetism and Geoelectricity*, *29*(4), 379–400. https://doi.org/10.5636/jgg.29.379

Bryson, J. F. J., Church, N. S., Kasama, T., & Harrison, R. J. (2014). Nanomagnetic intergrowths in Fe-Ni meteoritic metal: The potential for time-resolved records of planetesimal dynamo fields. *Earth and Planetary Science Letters*, *388*, 237–248. https://doi.org/10.1016/j.epsl.2013.12.004

Bryson, J. F. J., Herrero-Albillos, J., Kronast, F., Ghidini, M., Redfern, S. A. T., van der Laan, G., & Harrison, R. J. (2014). Nanopaleomagnetism of meteoritic Fe-Ni studied using X-ray photoemission electron microscopy. *Earth and Planetary Science Letters*, *396*, 125–133. https://doi.org/10.1016/j.epsl.2014.04.016

Bryson, J. F. J., Nichols, C. I. O., Herrero-Albillos, J., Kronast, F., Kasama, T., Alimadadi, H., et al. (2015). Long-lived magnetism from solidification-driven convection on the pallasite parent body. *Nature*, *517*(7535), 472–475. https://doi.org/10.1038/nature14114

Bryson, J. F. J., Weiss, B. P., Getzin, B., Abrahams, J. N. H., Nimmo, F., & Scholl, A. (2019). Paleomagnetic evidence for a partially differentiated ordinary chondrite parent asteroid. *Journal of Geophysical Research: Planets*, *124*, 1880–1898. https://doi.org/10.1029/2019JE005951

Bryson, J. F. J., Weiss, B. P., Harrison, R. J., Herrero-Albillos, J., & Kronast, F. (2017). Paleomagnetic evidence for dynamo activity driven by inward crystallisation of a metallic asteroid. *Earth and Planetary Science Letters*, *472*, 152–163. https://doi.org/10.1016/j.epsl.2017.05.026

Büttner, F., Lemesh, I., Schneider, M., Pfau, B., Günther, C. M., Hessing, P., et al. (2017). Field-free deterministic ultra-fast creation of magnetic skyrmions by spin-orbit torques. *Nature Nanotechnology*, *12*(11), 1040–1044. https://doi.org/10.1038/nnano.2017.178

Büttner, F., Moutafis, C., Schneider, M., Krüger, B., Günther, C. M., Geilhuffe, J., et al. (2015). Dynamics and inertia of skyrmionic spin structures. *Nature Physics*, *11*(3), 225–228. https://doi.org/10.1038/nphys3234

Einsle, J. F., Eggeman, A. S., Martineau, B. H., Saghi, Z., Collins, S. M., Blukis, R., et al. (2018). Nanomagnetic properties of the meteorite cloudy zone. *Proceedings of the National Academy of Sciences*, *115*, E11436. https://doi.org/10.1073/pnas.1809378115

Eisebitt, S., Lüning, J., Schlotter, W. F., Hellwig, O., Eberhardt, W., & Stöhr, J. (2004). Lensless imaging of magnetic nanostructures by X-ray. *Nature*, *432*(7019), 885–888. https://doi.org/10.1038/nature03139

Faigel, G., & Tegze, M. (1999). X-ray holography. *Reports on Progress in Physics*, *62*(3), 355–393. https://doi.org/10.1088/0034-4885/62/3/002

Fu, R. R., Weiss, B. P., Lima, E. A., Harrison, R. J., Bai, X. N., Desch, S. J., et al. (2014). Solar nebula magnetic fields recorded in the Semarkona meteorite. *Science*, *346*(6213), 1089–1092. https://doi.org/10.1126/science.1258022

Fu, R. R., Weiss, B. P., Shuster, D. L., Gattacceca, J., Grove, T. L., Suavet, C., et al. (2012). An ancient core dynamo in asteroid Vesta. *Science (New York, N.Y.)*, *338*(6104), 238–241. https://doi.org/10.1126/science.1225648

Gattacceca, J., Suavet, C., Rochette, P., Weiss, B. P., Winklhofer, M., Uehara, M., & Friedrich, J. M. (2014). Metal phases in ordinary chondrites: Magnetic hysteresis properties and implications for thermal history. *Meteoritics & Planetary Science*, *49*(4), 652–676. https://doi.org/10.1111/maps.12268

Geilhufe, J., Pfau, B., Günther, C. M., Schneider, M., & Eisebitt, S. (2020). Achieving diffraction-limited resolution in soft-X-ray Fourier-transform holography. *Ultramicroscopy*, *214*, 113005. https://doi.org/10.1016/j.ultramic.2020.113005

Günther, C. M., Hellwig, O., Menzel, A., Pfau, B., Radu, F., Makarov, D., et al. (2010). Microscopic reversal behavior of magnetically capped nanospheres. *Physical Review B: Condensed Matter and Materials Physics*, *81*, 1–7.

Guskova, Y. G. (1965). Investigation of the natural remanent magnetism of meteorites composed of iron and iron-stone (iron and iron-stone meteorites studied for natural remanent magnetism in inferences of outer space conditions). *Geomagnetism and Aeronomy*, *5*, 126–133.

Harrison, J. R., & Lascu, I. (2014). FORCulator: A micromagnetic tool for simulating first-order reversal curves. *Geochemistry, Geophysics, Geosystems*, *15*, 4671–4691. https://doi.org/10.1002/2014GC005582

Hauet, T., Günther, C. M., Pfau, B., Schabes, M. E., Thiele, J. U., Rick, R. L., et al. (2008). Direct observation of field and temperature induced domain replication in dipolar coupled perpendicular anisotropy films. *Physical Review B: Condensed Matter and Materials Physics*, *77*, 2–5.

Hellwig, O., Eisebitt, S., Eberhardt, W., Schlotter, W. F., Lüning, J., & Stöhr, J. (2006). Magnetic imaging with soft x-ray spectroholography. *Journal of Applied Physics*, *99*, 2004–2007.

Kim, D. H., Fischer, P., Chao, W., Anderson, E., Im, M. Y., Shin, S. C., & Choe, S. B. (2006). Magnetic soft X-ray microscopy at 15 nm resolution probing nanoscale local magnetic hysteresis (invited). *Journal of Applied Physics*, *99*, 2004–2007.

Maurel, C., Weiss, B. P., & Bryson, J. F. J. (2019). Meteorite cloudy zone formation as a quantitative indicator of paleomagnetic field intensities and cooling rates on planetesimals. *Earth and Planetary Science Letters*, *513*, 166–175. https://doi.org/10.1016/j.epsl.2019.02.027

Muxworthy, A. (2013). The role of magnetic interactions in natural systems. *Astronomy and Geophysics*, *54*, 31–35.

Muxworthy, A. R., Heslop, D., Paterson, G. A., & Michalk, D. (2011). A Preisach method for estimating absolute paleofield intensity under the constraint of using only isothermal measurements: 2. Experimental testing. *Journal of Geophysical Research*, *116*, B04103. https://doi.org/10.1029/2010JB007844

Néel, L., Pauleve, J., Pauthenet, R., Laugier, J., & Dautreppe, D. (1964). Magnetic properties of an iron-nickel single crystal ordered by neutron bombardment. *Journal of Applied Physics*, *35*(3), 873–876. https://doi.org/10.1063/1.1713516

Nichols, C. I. O., Bryson, J. F. J., Herrero-Albillos, J., Kronast, F., Nimmo, F., & Harrison, R. J. (2016). Pallasite paleomagnetism: Quiescence of a core dynamo. *Earth and Planetary Science Letters*, *441*, 103–112. https://doi.org/10.1016/j.epsl.2016.02.037

Nichols, C. I. O., Einsle, J. F., Im, M. Y., Kasama, T., Saghi, Z., Midgley, P. A., & Harrison, R. J. (2019). Field response of magnetic vortices in dusty olivine from the Semarkona Chondrite. *Geochemistry, Geophysics, Geosystems*, *20*, 1441–1453. https://doi.org/10.1029/2018GC008159

Nolle, D., Weigand, M., Audehm, P., Goering, E., Wiesemann, U., Wolter, C., et al. (2012). Unique characterization possibilities in the ultra high vacuum scanning transmission X-ray microscope (UHV-STXM) "MAXYMUS" using a rotatable permanent magnetic field up to 0.22 T. *Review of Scientific Instruments*, *83*, 046112. https://doi.org/10.1063/1.4707747

Pfau, B., & Eisebitt, S. (2015) *Synchrotron light sources and free-electron lasers*. Cham, Switzerland: Springer.

Pfau, B., Günther, C. M., Hauet, T., Hannen, T., Eisebitt, S., & Hellwig, O. (2014). Influence of stray fields on the switching-field distribution for bit-patterned media based on pre-patterned substrates. *Applied Physics Letters*, *105*, 132407. https://doi.org/10.1063/1.4896982

Qiu, Z. Q., & Bader, S. D. (2000). Surface magneto-optic Kerr effect. *Review of Scientific Instrumentation*, *71*(3), 1243–1255. https://doi.org/10.1063/1.1150496

Santos, F., Dowell, C. D., Houde, M., Looney, L., Lopez-Rodriguez, E., Novak, G., & Ward-Thompson, D. (2018). HAWC+/SOFIA observations of Rho Oph A: Far-infrared polarization spectrum [Abstract]. American Astronomical Society Meeting Abstracts, 231.

Sarid, D. (1994) *Scanning force microscopy: With applications to electric, magnetic and atomic forces*. New York, NY: Oxford University Press.

Schaffer, M., Schaffer, B., & Ramasse, Q. (2012). Sample preparation for atomic-resolution STEM at low voltages by FIB. *Ultramicroscopy*, *114*, 62–71. https://doi.org/10.1016/j.ultramic.2012.01.005

Scott, E. R. D. (1973). The nature of dark-etching rims in meteoritic taenite. *Geochimica et Cosmochimica Acta*, *37*(10), 2283–2294. https://doi.org/10.1016/0016-7037(73)90104-X

Shah, J., Bates, H. C., Muxworthy, A. R., Hezel, D. C., Russell, S. S., & Genge, M. J. (2017). Long-lived magnetism on chondrite parent bodies. *Earth and Planetary Science Letters*, *475*, 106–118. https://doi.org/10.1016/j.epsl.2017.07.035

Shah, J., Williams, W., Almeida, T. P., Nagy, L., Muxworthy, A. R., Kovács, A., et al. (2018). The oldest magnetic record in our solar system identified using nanometric imaging and numerical modeling. *Nature Communications*, *9*, 9–14.

Shcherbakov, V. P., Lamash, B. E., & Sycheva, N. K. (1995). Monte-Carlo modelling of thermoremanence acquisition in interacting single-domain grains. *Physics of the Earth and Planetary Interiors*, *87*(3-4), 197–211. https://doi.org/10.1016/0031-9201(94)02969-I

Shcherbakov, V. P., & Sycheva, N. K. (1996). Monte Carlo modelling of TRM and CRM acquisition and comparison of their properties in an ensemble of interacting SD grains. *Geophysical Research Letters*, *23*(20), 2827–2830. https://doi.org/10.1029/96GL01999

Simon, J. B., Bai, X. N., Armitage, P. J., Stone, J. M., & Beckwith, K. (2013). Turbulence in the outer regions of protoplanetary disks. II. Strong accretion driven by a vertical magnetic field. *Astrophysical Journal*, *775*, 73. https://doi.org/10.1088/0004-637X/775/1/73

Stroke, G. W. (1965). Lenseleff Fourier-transform method for optical holography. *Applied Physics Letters*, *6*(10), 201–203. https://doi.org/10.1063/1.1754131

Wang, H., Weiss, B. P., Bai, X. N., Downey, B. G., Wang, J., Wang, J., et al. (2017). Lifetime of the solar nebula constrained by meteorite paleomagnetism. *Science*, *355*(6325), 623–627. https://doi.org/10.1126/science.aaf5043

Wardle, M. (2007). Magnetic fields in protoplanetary disks. *Astrophysics and Space Science*, *311*(1-3), 35–45. https://doi.org/10.1007/s10509-007-9575-8

Winthorp, J. T., & Worthing, C. R. (1965). X-ray microscopy by successive Fourier tranformation. *Physics Letters*, *15*(2), 124–126. https://doi.org/10.1016/0031-9163(65)91304-1

Yang, C. W., Williams, D. B., & Goldsteini, J. I. (1997). A new empirical cooling rate indicator for meteorites based on the size of the cloudy zone of the metallic phases. *Meteoritics & Planetary Science*, *32*(3), 423–429. https://doi.org/10.1111/j.1945-5100.1997.tb01285.x

Yeem, K. E. S., & Harrison, R. J. (2019). Interaction-drive domain-state transition in the meteoritre cloudy zone: A hybrid micromagnetic approach to modelling remanence acquisition. Paper presented at American Geophysical Union, Fall Meeting 2019.